

Donwilhelmsite, [CaAl₄Si₂O₁₁], a new lunar high-pressure Ca-Al-silicate with relevance for subducted terrestrial sediments

DOI:

[10.2138/am-2020-7393](https://doi.org/10.2138/am-2020-7393)

Document Version

Accepted author manuscript

[Link to publication record in Manchester Research Explorer](#)

Citation for published version (APA):

Fritz, J., Greshake, A., Klementova, M., Wirth, R., Palatinus, L., Trønnnes, R. G., A. Fernandes, V., Böttger, U., & Ferrière, L. (2020). Donwilhelmsite, [CaAl₄Si₂O₁₁], a new lunar high-pressure Ca-Al-silicate with relevance for subducted terrestrial sediments. *American Mineralogist*. <https://doi.org/10.2138/am-2020-7393>

Published in:

American Mineralogist

Citing this paper

Please note that where the full-text provided on Manchester Research Explorer is the Author Accepted Manuscript or Proof version this may differ from the final Published version. If citing, it is advised that you check and use the publisher's definitive version.

General rights

Copyright and moral rights for the publications made accessible in the Research Explorer are retained by the authors and/or other copyright owners and it is a condition of accessing publications that users recognise and abide by the legal requirements associated with these rights.

Takedown policy

If you believe that this document breaches copyright please refer to the University of Manchester's Takedown Procedures [<http://man.ac.uk/04Y6Bo>] or contact openresearch@manchester.ac.uk providing relevant details, so we can investigate your claim.



Fritz, J., Greshake, A., Klementova, M., Wirth, R., Palatinus L. L. , Trønnes, R. G., Assis
Fernandes, V., Böttger, U., Ferrière, L, 2020. Donwilhelmsite, $[\text{CaAl}_4\text{Si}_2\text{O}_{11}]$, a new lunar high-
pressure Ca-Al-silicate with relevance for subducted terrestrial sediments. *American Mineralogist*.
<https://doi.org/10.2138/am-2020-7393>

**Donwilhelmsite, $[\text{CaAl}_4\text{Si}_2\text{O}_{11}]$, a new lunar high-pressure Ca-Al-silicate with relevance for
subducted terrestrial sediments**

Jörg Fritz^{1,2}, Ansgar Greshake³, Mariana Klementova⁴, Richard Wirth⁵, Lukas Palatinus⁴, Reidar
G. Trønnes⁶, Vera Assis Fernandes^{3,7}, Ute Böttger⁸, and Ludovic Ferrière⁹

¹Zentrum für Rieskrater und Impaktforschung, Nördlingen, Vordere Gerbergasse 3
86720 Nördlingen, Germany

²Saalbau Weltraum Projekt, Liebigstraße 6, D-64646 Heppenheim, Germany

³Museum für Naturkunde Berlin, Invalidenstraße 43, D-10115 Berlin, Germany

⁴Institute of Physics of the Czech Academy of Science, v.v.i., Na Slovance 2, 182 21 Prague,
Czech Republic

⁵Helmholtz-Zentrum Potsdam - Deutsches GeoForschungsZentrum, Sektion 3.5 Grenzflächen-
Geochemie, Telegrafenberg, D-14473 Potsdam, Germany

⁶Natural History Museum and Centre for Earth Evolution and Dynamics (CEED), University of
Oslo, N-0315 Oslo, Norway

⁷Department of Earth and Environmental Sciences, University of Manchester, Williamson
Building, Oxford Road, M13 9PL Manchester, United Kingdom

⁸Institut für Optische Sensorsysteme, Deutsches Zentrum für Luft und Raumfahrt Berlin,
Rutherfordstraße 2, D-12489 Berlin, Germany

⁹Natural History Museum, Burgring 7, A-1010 Vienna, Austria

E-mail of corresponding author: joerg.fritz@kino-heppenheim.de

ABSTRACT

29 We report on the occurrence of a new high-pressure Ca-Al-silicate in localized shock melt pockets
30 found in the feldspathic lunar meteorite Oued Awlitis 001 and discuss the implications of our
31 discovery. The new mineral crystallized as tiny, micrometer sized, acicular grains in shock-melt
32 pockets of roughly anorthitic bulk composition. Transmission electron microscopy based 3
33 dimension electron diffraction (3D ED) revealed that the $\text{CaAl}_4\text{Si}_2\text{O}_{11}$ crystals are identical to the
34 calcium aluminum silicate, CAS, phase first reported from static pressure experiments. The new
35 mineral has a hexagonal structure, with a space group of $P6_3/mmc$ and lattice parameters of $a =$
36 $5.42(1) \text{ \AA}$; $c = 12.70(3) \text{ \AA}$; $V = 323(4) \text{ \AA}^3$; $Z = 2$. This is the first time 3D ED was applied to
37 structure determination of an extraterrestrial mineral. The International Mineralogical Association
38 has approved this naturally formed CAS phase as the new mineral “donwilhelmsite” [$\text{CaAl}_4\text{Si}_2\text{O}_{11}$],
39 honoring the lunar US geologist Don E. Wilhelms. On the Moon, donwilhelmsite can form from
40 the primordial feldspathic crust during impact cratering events. In the feldspathic lunar meteorite
41 Oued Awlitis 001 needles of donwilhelmsite crystallized in $\sim 200 \text{ \mu m}$ in size shock melt pockets of
42 anorthositic-like chemical composition. These melt pockets quenched within milliseconds during
43 declining shock pressures. Shock melt pockets in meteorites serve as natural crucibles mimicking
44 the conditions expected in the Earth’ mantle. Donwilhelmsite forms in the Earths’ mantle during
45 deep recycling of aluminous crustal materials, where it is a key host for Al and Ca of subducted
46 sediments in most of the transition zone and in the uppermost lower mantle (460-700 km).
47 Donwilhelmsite bridges the mineralogical gap between kyanite and the Ca-component of
48 clinopyroxene at low pressures and the Al-rich Ca-ferrite phase and Ca-perovskite at high-
49 pressures. In ascending buoyant mantle plumes, at about 460 km depth, donwilhelmsite is expected
50 to break down into minerals such as garnet, kyanite, and clinopyroxene. This may trigger minor

partial melting releasing a range of incompatible minor and trace elements contributing to the enriched mantle (EM1 and EM2) components associated with subducted sedimentary lithologies.

Keywords: High-pressure phase, new mineral, donwilhelmsite, Oued Awlitis 001 lunar meteorite, shock metamorphism, subduction, mantle mineral, enriched mantle component

INTRODUCTION

The Earth's continental crust and the lunar highlands (i.e., consisting of material derived from many superposed impact ejecta from all crustal levels and covering the lunar surface) are dominantly felsic in composition, including as major elements, O, Si, Al, Ca, Na, and K. Minerals controlling the distribution of these elements are important agents for the origin and fate of planetary crusts. Remnants of a primordial crust are preserved on the Moon, showing the intense mechanical and thermal metamorphism and melting, caused by impacts during the Heavy Bombardment Eon (Wilhelms 1987; Fernandes et al. 2013). Nonetheless, these remnants document initial planetary differentiation processes. Fifty years ago, the Apollo 11 mission collected 21.6 kg of lunar rocks and soils, including anorthosites composed of >90 vol% plagioclase (Wilhelms 1987, 1993). Lunar anorthosites contain exceptionally high proportions of the Ca-rich anorthite endmember of the albite – anorthite ($\text{Na}[\text{AlSi}_3\text{O}_8] - \text{Ca}[\text{Al}_2\text{Si}_2\text{O}_8]$) plagioclase solid solution, with 96-98 mol% anorthite. From these samples, it was concluded that the impact gardened bright lunar highlands derived from a primordial (>4.3 Ga old) anorthositic crust, several tens of kilometers thick (50 ± 15 km, e.g., Wiczorek et al. 2006) that crystallized and floated on a dense lunar magma ocean, several hundred kilometers deep (Wood et al. 1970; Smith et al. 1970).

72 Preservation of a highly fragmented and displaced primary crust (>4.4 Ga), as well as primary
73 mantle heterogeneities resulting from the crystallization of the, likely heterogeneous, lunar magma
74 ocean, is in stark contrast to the geologically active Earth. Earth's oldest preserved oceanic and
75 continental crusts are about 0.2 and 4.0 Gy old, respectively, with the latter being found in very
76 limited areas on Earth. During plate tectonic processes, crustal materials rich in volatiles and other
77 elements incompatible in mantle minerals are reintroduced into the depleted mantle by subduction.
78 The sinking oceanic plates carry continental-derived sediments into the deep mantle (Irifune et al.
79 1994; Plank and Langmuir 1998), and the enriched mantle component EM2 (enriched mantle 2;
80 with high $^{87}\text{Sr}/^{86}\text{Sr}$ and intermediate $^{206}\text{Pb}/^{204}\text{Pb}$) is ascribed to the direct terrigenous component
81 with a composition similar to the upper continental crust (White 2015). In contrast, the origin of
82 the enriched mantle component EM1 (enriched mantle 1; with intermediate $^{87}\text{Sr}/^{86}\text{Sr}$ and low
83 $^{206}\text{Pb}/^{204}\text{Pb}$) is more elusive but often attributed to pelagic sediments (Garapić et al. 2015).
84 Especially Archean-aged sediments are good candidates for the enriched components in the mantle
85 source of South Pacific Ocean islands like Pitcairn (Delavault et al. 2016). About 75% of the
86 subducted sediment flux is estimated to be direct terrigenous material of average upper crust
87 composition (Plank and Langmuir 1998). Such lithologies can be recycled into the lower mantle
88 and retained there for up to 2-3 Gy, before being sampled by recent plumes and ongoing ocean
89 island volcanism. Deep recycling of continentally derived sediments below 200-300 km depth is
90 facilitated by stepwise densification at 6.5 GPa (~ 200 km depth), when orthoclase breaks down,
91 and at 9 GPa (~ 280 km depth), when hollandite and stishovite form, to densities exceeding that of
92 ambient peridotite at the 280-700 km depth range (Irifune et al. 1994). At deeper levels, the
93 sediment and peridotite densities may remain nearly identical to depths beyond 1200 km and ~ 40
94 GPa (Poli and Schmidt 2002). The densification of terrigenous and pelagic sedimentary lithologies

95 in the mantle transition zone is aided by the occurrence of 7-10 % of a Ca-Al-silicate (CAS) phase
96 with composition $\text{CaAl}_4\text{Si}_2\text{O}_{11}$ at the 460-700 km depth range (Irifune et al. 1994).

97 Natural examples of those minerals composing Earths' deep mantle are rarely accessible. Many
98 minerals stable at deep mantle pressure and temperature conditions decompose into other mineral
99 assemblages stable at lower pressures due to the specific pressure-temperature-time (P-T-t) path
100 during ascent. Notable exceptions include high-pressure phases such as ringwoodite (high-pressure
101 polymorph of olivine), ferropericlase, and Mg-wüstite found as inclusions in diamonds (e.g.,
102 Pearson et al. 2014). The diamond host serves as a pressure vault providing an environment that
103 allows deep mantle high-pressure mineral inclusions to cool to temperatures low enough to inhibit
104 a back reaction into low-pressure mineral assemblages. Localized zones of shock melt in
105 moderately to strongly shocked meteorites present another natural environment in which a hot and
106 compressed melt is quenched at typical deep mantle pressures to temperatures low enough to inhibit
107 a back reaction into low-pressure mineral assemblages during pressure release (Chen et al. 1996;
108 Fritz et al. 2017). A great diversity of natural examples of high-pressure minerals, analogous to
109 those occurring in the Earths' mantle, were first found in local shock melt zones (such as melt veins
110 and melt pockets) of different types of meteorites, including chondrites and achondrites of basaltic
111 and dunitic compositions (e.g., Tomioka and Miyahara 2017). Compared to mafic and ultramafic
112 meteorites, reports of shock melt zones in felsic meteorites are very limited. Although CAS-like
113 phases of various compositions close to the $\text{CaAl}_4\text{Si}_2\text{O}_{11}$ - $\text{NaAl}_3\text{Si}_3\text{O}_{11}$ joint have been found in
114 shocked basaltic meteorites from Mars (i.e., in shergottites, Beck et al. 2004; El Goresy et al. 2013),
115 the CAS phase has neither been characterized in felsic meteorites, nor been officially named. Here
116 we report on the discovery and detailed characterization of the natural high-pressure and high-
117 temperature transformation of anorthite in shock melt zones within the feldspathic lunar meteorite
118 Oued Awlitis 001.

MATERIAL AND METHODS

Oued Awlitis 001 meteorite

The main fragment of the lunar meteorite Oued Awlitis 001, originally 382 g, was found on January 15, 2014, in the Western Sahara (25.954°N, 12.493°W). It is largely covered with a green to brownish fusion crust showing features of orientation. Another fragment, 50.5 g, fitting the larger one, was found a few weeks later. About 60% of the recovered meteorite is covered with a crackled fusion crust and shows a rollover lip on one side. Oued Awlitis 001 is classified as an anorthositic lunar impact melt rock, composed of large anorthite clasts set in a poikilitic matrix of plagioclase, olivine, and pyroxene (Ferrière et al. 2017; Ruzicka et al. 2017; Wittmann et al. 2019). The poikilitic matrix indicates a slow cooling history, possibly in a ~100 meter thick impact melt sheet (Wittmann et al. 2019). Later impact event(s) emplaced the rock closer to the lunar surface, and about 0.3 Ma ago it was impact accelerated beyond lunar escape velocity and delivered to Earth (see Ferrière et al. 2017; Wittmann et al. 2019). The sections investigated in this study were prepared from the 50.5 g fragment of this meteorite from the Natural History Museum Vienna (NHMV, Austria) collection (specimen NHMV-N9830).

Optical microscopy

A thin section of Oued Awlitis 001 (NHMV-O105), prepared from the pristine part of the meteorite (i.e., excluding the fusion crust) was studied in transmitted light at the NHMV. A polished thick section mounted in epoxy (NHMV-O104) was studied by optical microscopy in reflected light aided by the use of immersion oil at the Museum für Naturkunde, Berlin, Germany. Such an approach is ideal to recognize potential high-pressure phases within local shock melt zones inside meteorites, as minerals and glass display intense brightness contrast in reflected light. This thick

section was then studied using a binocular microscope, to acquire depth information of the transparent minerals and their outer surface, visible through the transparent epoxy mount.

Micro-Raman spectroscopy

Subsequently, micro-Raman spectroscopic analyses were conducted on the uncoated thick section and prior to any disturbances caused by electron beam irradiation during electron microscopic investigations. Raman spectra were collected with the WITec Alpha 300 Raman confocal microscope at the Deutsches Zentrum für Luft und Raumfahrt (DLR), Berlin, Germany, using a Nd:YAG laser with an excitation wavelength of 532 nm, a 100x magnification objective (NA 0.8), and a power of 3 to 7 mW on the sample.

Electron microscopy

Backscattered electron (BSE) microscopic images were obtained on the polished and carbon coated thick section at the Museum für Naturkunde Berlin (MfN), Germany, using a JEOL JXA 8500F Field Emission Microprobe. For X-ray elemental maps, the microprobe was operated with 15 kV accelerating voltage, a 15 nA beam current, an about 10 nm beam size, and a dwell times of 100 ms. Quantitative chemical analyses of the shock melt pocket were obtained with the same instrument using a 10–15 kV accelerating voltage, a 15 nA beam current, and a defocused 10 µm diameter beam. Suitable glass and mineral standards certified by the Smithsonian Museum were used as reference samples for electron microprobe analysis (Jarosewich et al. 1980).

Focused Ion Beam (FIB)

163 FIB foils 20 x 10 x 0.15 μm in size were cut out of the thick section at the Deutsches
164 GeoForschungsZentrum, Sektion 3.5 Grenzflächen-Geochemie Helmholtz-Zentrum (GFZ)
165 Potsdam, Germany, using a FEI TEM 200 FIB system.

166

167 **Transmission electron microscopy (TEM)**

168 Initial TEM characterization was performed using a FEI TecnaiTM G2 F20 X-Twin operated at 200
169 kV with a field emission gun electron source at GFZ Potsdam. The microscope is equipped with
170 an EDAX ultra-thin window EDX system, a Fishione high-angle annular dark-field (HAADF)
171 detector, and a post-column Gatan imaging filter (GIF Tridiem).

172 Additional TEM characterization, including chemical analyses and crystal structure determination,
173 was performed at the Institute of Physics of the Czech Academy of Science (IPCAS), Prague,
174 Czech Republic. The reported chemical analyses were obtained using an FEI TecnaiTM G2 F20 X-
175 Twin attached with an EDAX energy dispersive spectrometer (EDS) operated at 200 kV. The
176 chemical analyses were obtained with a defocused beam with the size of about 300 nm in diameter
177 in TEM mode to avoid the loss of volatile elements such as sodium. Standardless quantification
178 using FEI TIA software version 4.2 was used for the analysis. The empirical formula was calculated
179 on the basis of 7 cations.

180 The crystal structure of donwilhelmsite was determined by 3D electron diffraction (3D ED; Gemmi
181 et al. 2019 and references therein) performed on a Philips CM 120 (LaB₆, 120kV), equipped with
182 a NanoMEGAS precession unit DigiStar and an Olympus SIS CCD camera Veleta (2048 x 2048
183 px), in Prague. The diffraction data were collected by means of precession electron diffraction
184 (Mugnaioli et al. 2009). The target crystal was sequentially tilted by 1 deg. step from -50 to +50
185 deg., and at every tilt step a precession diffraction pattern in micro-diffraction mode was acquired

using a precession angle of 1 deg. Data processing was carried out using the PETS software (Palatinus et al. 2019). Structure solution and refinement were performed using the computing system Jana2006 (Petříček et al. 2014). The structure was solved by the charge flipping algorithm using the program Superflip (Palatinus and Chapuis 2007), and refined using a dynamical approach (Palatinus et al. 2015a, 2015b).

RESULTS

The feldspathic lunar meteorite Oued Awlitis 001 (Fig. 1) is an impact melt rock predominantly composed of up to about 5 mm-sized Ca-rich plagioclase clasts set into a crystallized melt groundmass composed of <100 μm sized olivine and pyroxene grains poikilitically enclosing equally sized anorthite grains. All silicates display strong compositional zoning. Minor phases present include FeNi metal, troilite, ilmenite, Ti-rich spinel, apatite, zircon, baddeleyite, and silica. For the detailed petrology and mineral chemistry of the meteorite the reader is referred to Ferrière et al. (2017) and Wittmann et al. (2019).

Oued Awlitis 001 is moderately shocked. The observed shock metamorphic effects developed during a later impact event which affected the already fully crystalline impact melt rock. Plagioclase is mostly crystalline, showing undulatory extinction, reduced birefringence, and well-developed planar deformation features (PDF). In a few places, the plagioclase is transformed into diaplectic glass, so-called maskelynite.

Locally, the meteorite contains thin shock melt veins ranging from 50 to 150 μm in thickness, as well as shock melt pockets with diameter typically of about 200 μm (Fig. 2a). Optical inspection with a binocular microscope showed that the melt veins are three dimensional melt sheets with irregular surfaces extending deep into the meteorite sample. The melt veins are recrystallized to

extremely fine-grained mineral assemblages. In contrast, the melt pockets appear isolated and contain bundles (acicular texture) of up to 20 μm long and less than 1 μm wide needles that crystallized from the melt (Fig. 2b). Electron microprobe investigation revealed that the shock melt pockets are roughly anorthitic in bulk composition (Table 1). In high-contrast BSE images (Fig. 2a-b), the acicular crystals appear slightly brighter than the matrix and are surrounded by a comparatively darker halo when compared to the adjacent anorthite shock melt. Elemental maps show that the needle shaped crystals are enriched in Al and slightly depleted in Ca compared to the glass in the shock melt pocket (Fig. 3). The needles do not incorporate Fe and Mg (the Mg map is not shown). The compositional differences between glass and crystals are such that these phases can be easily overlooked in low-contrast BSE surveys. The localized zones of shock melt and the potential presence of crystallized minerals in polished samples can be identified quickly via reflected light microscopy. In a piece of Oued Awlitis 001 with a polished surface of $\sim 5 \times 5$ mm in size a total of three shock melt pockets and one shock melt vein were observed. The needle shaped minerals crystallized from all three isolated, roundish, shock melt pockets, but are not observed in the shock melt vein, the latter apparently represents a three dimensional melt sheet.

These needle-shaped crystals provided Raman spectra with peaks at 280, 420, 500, 618, and 912 cm^{-1} (Fig. 4), and a shoulder indicating an additional peak at ~ 850 cm^{-1} . The Raman spectra obtained from the needles are in good agreement with Raman spectra reported for synthetic $\text{CaAl}_4\text{Si}_2\text{O}_{11}$ with characteristic peaks at 280, 422, 486, 616, 851, and 910 cm^{-1} Raman shift (Beck et al. 2004). The broad band at 1015 cm^{-1} , together with some contribution around 460-550 cm^{-1} , is interpreted to be from the Ca-, Al-, and Si-rich glass surrounding the crystals. A 1015 cm^{-1} band was also observed and relates to the non-bridging vibrations of TO_4 tetrahedra (where T = Si, Al), and its position indicates preferentially more non-bridging Si-O than Al-O tetrahedra compared to anorthite glass with a band at 985 cm^{-1} (Sharma et al. 1983; Matson et al. 1986). The shock melt

pocket of anorthite-like composition (Table 1) displays Raman spectra with a broad feature around 985 cm^{-1} (Fig. 4). In BSE images the brighter needles are surrounded by a dark halo. The halo is Al-depleted and Si-enriched compared to the anorthitic shock melt pocket, due to crystallization of the Al-rich needle-shaped crystals (Table 1). The halo contains 20 wt% Al_2O_3 suggesting an incomplete crystallization sequence. Notably, the glass is not dissociated in phases such as SiO_2 , CaO or CaSiO_3 , as revealed by the absence of Raman features in the $\sim 800 \text{ cm}^{-1}$ spectral region typical for SiO_2 glass.

Transmission electron microscopy investigation showed that all needles are embedded in a completely amorphous glassy matrix. No other minerals, such as garnet, corundum, kyanite, or stishovite were found in the studied shock melt pockets with TEM investigations, elemental maps, and Raman spectroscopic surveys. An average of ten TEM EDS-analyses of the CAS needles yielded a chemical composition of 52.7 wt% Al_2O_3 , 32.6 wt% SiO_2 , and 15.0 wt% CaO (Table 2). The empirical formula calculated on the basis of 7 cations is $\text{Ca}_{1.02}\text{Al}_{3.92}\text{Si}_{2.06}\text{O}_{11}$. The analytical results show full occupation of Ca and only very slight excess of Si and deficiency of Al with respect to the stoichiometric composition. Sodium, K, Mg, and Fe contents are below the detection limit of about 1 wt%.

The crystal structure of the new mineral was determined from eight datasets obtained with TEM using 3D ED (Fig. 5; Table 3). The lattice parameters are $a = 5.42(1) \text{ \AA}$; $c = 12.70(3) \text{ \AA}$; $V = 323(4) \text{ \AA}^3$; $Z = 2$. The hexagonal structure with a space group of $P6_3/mmc$ is identical to that of the CAS phase synthesized at pressures $>14 \text{ GPa}$ and temperatures $>1773 \text{ K}$ (Table 3; Irifune et al. 1994; Gautron et al. 1999). Moreover, the atomic distribution, inferred from the combination of bond distances and bond valence sums, is also identical (Table 4). The results presented here are from

the dataset 180520-2, which was refined dynamically to $R1(obs) = 8.95\%$ (Table 5). The crystal structure is composed of di-octahedral M1 layers containing Al and Si in 1:2 proportion, and an interlayer consisting of M2 octahedral positions fully occupied by Al, tetrahedral (T) positions half occupied by Al, and larger cavities occupied by Ca (Fig. 6). The tetrahedral position T-Al3 is disordered between two positions. An ordered model can be built with only one of the two positions occupied. The space group of such a model is $P6_3mc$, and its refinement gave slightly increased figures of merit. This result confirms that the structure is indeed centro-symmetric with a disordered tetrahedral position. The chemical composition derived from the structure model is $CaAl_4Si_2O_{11}$, in good agreement with the measured chemical composition of $Ca_{1.02}Al_{3.92}Si_{2.06}O_{11}$.

DISCUSSION

The natural CAS phase ($CaAl_4Si_2O_{11}$) presented in this study is named donwilhelmsite (IMA2018-113; Fritz et al. 2019a), and the holotype is catalogued as NHMV-O104 and preserved in the meteorite collection of the NHMV. Donwilhelmsite is named to honor Dr. Don E. Wilhelms for his seminal and ground-breaking work on the geological history of the Moon (Wilhelms 1987, 1993).

Donwilhelmsite [$CaAl_4Si_2O_{11}$] was identified within the lunar meteorite Oued Awlitis, 001, and the structure was solved by 3D electron diffraction. The needle shaped minerals are structurally and chemically identical to the CAS phase, first synthesized in static pressure experiments by Irifune et al. (1994), and later characterized in detail by Gautron et al. (1999). Similar and more Na-rich examples of the $CaAl_4Si_2O_{11} - NaAl_3Si_3O_{11}$ solid solution series were previously reported from shock melt veins in basaltic Martian meteorites (Beck et al. 2004). The Na-rich endmember ($NaAl_3Si_3O_{11}$) is energetically in disfavor compared to jadeite or calcium ferrite and, thus, unlikely

to form (Akaogi et al. 2010). The phases along the $\text{CaAl}_4\text{Si}_2\text{O}_{11}$ – $\text{NaAl}_3\text{Si}_3\text{O}_{11}$ solid solution series are Al-rich and Si-poor compared to the $\text{CaAl}_2\text{Si}_{3.5}\text{O}_{11}$ high-pressure phase zagamiite (Ma and Tschauner 2017; Ma et al. 2017). Donwilhelmsite forms a complex solid solution series with multiple cation substitution mechanisms including Fe, Mg, K, and Na (Irifune et al. 1994; Beck et al. 2004; Akaogi et al. 2010; El Goresy et al. 2013).

In the feldspathic lunar meteorite Oued Awlitis 001, the shock effects in plagioclase (Ferrière et al. 2017; Wittmann et al. 2019) indicate whole rock shock pressures of 20-24 GPa (Fritz et al. 2019b). The resulting shock-induced temperature increase of less than 100 K provides sufficiently low whole rock temperatures after shock decompression for the preservation of high-pressure phases when pressure almost instantly drops to zero pressure conditions (Fritz et al. 2017). In the up to 200 μm diameter sized isolated shock melt pockets, the shock pressure and temperature, preserved for a short time (milliseconds), mimic the pressure and temperature conditions in parts of the Earth's mantle. In the short period of declining temperature and pressure, donwilhelmsite grains crystallized from the melt. An Al_2O_3 content of ~20 wt% in the glass surrounding donwilhelmsite indicates an incomplete crystallization sequence, and the high Al-abundance suppressed the formation of the SiO_2 high-pressure polymorph stishovite.

On Earth, donwilhelmsite (the CAS phase, $\text{CaAl}_4\text{Si}_2\text{O}_{11}$) is an important mineral in continental-derived sediments subducted into the deep mantle. Static pressure experiments showed that the minimum pressure to form donwilhelmsite is 13 GPa for a $\text{CaAl}_4\text{Si}_2\text{O}_{11}$ composition (Akaogi et al. 2009) and 12 GPa for a less aluminum-rich lunar anorthositic-like composition (Nishi et al. 2018). For compositions corresponding to terrigenous sediments and upper continental crust, donwilhelmsite becomes stable at a pressure of 15.6 GPa (460 km depth) along the transition zone

of the adiabatic curve (Irifune et al. 1994; Stixrude et al. 2009). Donwilhelmsite was also recorded in basaltic compositions in near- and super-solidus conditions at about 26 GPa (Hirose and Fei 2002), and up to 3% of the mineral might be present in basalts in the lowermost 100 km of the transition zone at temperatures near and above the ambient mantle adiabatic curve (Litasov and Ohtani 2005).

Whereas the mineral with a bulk composition of $\text{CaAl}_4\text{Si}_2\text{O}_{11}$ (Akaogi et al. 2009) persists to about 36 GPa (950 km depth), at ambient adiabatic conditions (Stixrude et al. 2009) its stability is limited to about 30 GPa (810 km depth) for a composition resembling lunar anorthosites (Nishi et al. 2018). The pressure regime of the Earth's mantle, however, prevents the formation of primary anorthositic magma ocean crust and the accumulation of dense residual melts and associated cumulates in the uppermost mantle (Trønnes et al. 2019). On Earth, aluminum, volatiles, and other elements incompatible in mantle minerals are recycled into the deep mantle via terrigenous and pelagic sediments that plunge down with sinking oceanic plates (Irifune et al. 1994; Plank and Langmuir 1998).

Within its stability range of about 460-700 km depth, donwilhelmsite comprises 7-10% of terrigenous sediments subducted into the deep mantle and is an important reservoir for Al, Ca, Na, K, and other large-ion lithophile trace elements (Irifune et al. 1994; Litasov and Ohtani 2005). The decompression breakdown in ascending mantle plumes of donwilhelmsite into minerals such as garnet, kyanite, and clinopyroxene might trigger minor partial melting at about 460 km deep, releasing a range of incompatible minor and trace elements. Such melts could be important agents of mantle metasomatism and contribute to the composition of ocean island basalts and kimberlites.

IMPLICATIONS

Donwilhelmsite [CaAl₄Si₂O₁₁], is a new high-pressure Ca-Al-silicate found in shock melt pockets in the feldspathic lunar meteorite Oued Awlitis 001. The crystal structure of donwilhelmsite was solved with precession assisted 3D ED. The 3D ED approach to solve the crystal structure of minerals, first used by Rozhdestvenskaya et al. (2010), is now often applied to characterize synthetic high-pressure phases of geological interest (Gemmi et al. 2016). Here, for the first time, 3D ED technique is used to characterize an extraterrestrial mineral. The method provides new opportunities to study the great variety of minerals with submicrometer size that formed in a broad range of exotic environments (with varying P-T-t) as represented in some meteorites, and in material brought to Earth by “sample-return” space missions.

The identification of donwilhelmsite in a lunar meteorite underlines that high-pressure phase formation in localized zones of shock melt in meteorites is a common phenomenon. Meteorites serve as ideal natural crucibles for high-pressure mineral research because 1) they can provide localized zones of shock melt with a broad range of chemical and mineralogical properties, and 2) they were protected from various types of alteration processes in the space environment.

The natural occurrence of high-pressure phases is an important asset to understand geological processes affecting the magmatic evolution of terrestrial planets, such as phase-transformations in planetary interiors, magma ocean crystallisation, and plate tectonics. In the Earth’s mantle, donwilhelmsite forms during deep recycling of aluminous crustal materials, which in addition are rich in volatiles and other elements incompatible in mantle minerals. In the terrestrial rock cycle, donwilhelmsite is an important agent for transporting crustal sediments through the transition zone and uppermost lower mantle (460-700 km). . The decompression breakdown of donwilhelmsite in pelagic and terrigenous derived components in ascending mantle plumes contributes to the EM1 and EM2 geochemical signatures recognized in various mantle derived volcanic lithologies.

ACKNOWLEDGEMENTS

The crystallographic part of this study was performed using instruments of the ASTRA laboratory established within the Operation program Prague Competitiveness (project CZ.2.16/3.1.00/24510), and the infrastructure CzechNanoLab under project LM2018110 of the Czech Ministry of Education, Youth and Sports. We acknowledge financial support for VAF through the DFG research grant FE 1523/3-1 and via a Marie Skłodowska Curie Fellow, funded by the EU-Commission, HORIZON2020 Programme, project number 749815. CEED is funded by CoE-grant 223272 from the Research Council of Norway. Skillful FIB preparation by Anja Schreiber (GFZ) is greatly acknowledged. The thin and thick sections of the Oued Awilits 001 meteorite investigated here were prepared by Goran Batic (NHMV). The meteorite fragment was acquired by the NHMV thanks to money raised in a crowdfunding campaign by L.F. and with generous support from The Barringer Crater Company. We thank Victor Sharygin, an anonymous reviewer, and the technical editor for helpful reviews that improved the quality of this contribution.

REFERENCES CITED

- Akaogi, M., Haraguchi, M., Nakanishi, K., Ajiro, H., and Kojitani, H. (2010) High-pressure phase relations in the system $\text{CaAl}_4\text{Si}_2\text{O}_{11}$ – $\text{NaAl}_3\text{Si}_3\text{O}_{11}$ with implication for Na-rich CAS phase in shocked Martian meteorites. *Earth and Planetary Science Letters*, 289, 503–508. doi.org/10.1016/j.epsl.2009.11.043
- Akaogi, M., Haraguchi, M., Yaguchi, M., and Kojitani, H. (2009) High-pressure phase relations and thermodynamic properties of $\text{CaAl}_4\text{Si}_2\text{O}_{11}$ CAS phase. *Physics of the Earth and Planetary Interiors*, 173, 1–6. doi.org/10.1016/j.pepi.2008.10.010

371 Beck, P., Gillet, P., Gautron, L., Daniel, I., and El Goresy, A. (2004) A new natural high-pressure
 372 (Na,Ca)-hexaluminosilicate $[(Ca_xNa_{1-x})Al_{3+x}Si_{3-x}O_{11}]$ in shocked Martian meteorites. Earth
 373 and Planetary Science Letters, 219, 1–12. [doi.org/10.1016/S0012-821X\(03\)00695-2](https://doi.org/10.1016/S0012-821X(03)00695-2)

374 Chen M., Sharp T.G., El Goresy A., Wopenka B., and Xie X. (1996) The majorite pyrope
 375 magnesiowustite assemblage: Constraints on the history of shock veins in chondrites.
 376 Science, 271, 1570–1573. doi.org/10.1126/science.271.5255.1570

377 Delavault, H., Chauvel, C., Thomassot, E., Devey, C. W., and Dazas, B. (2016) Sulfur and lead
 378 isotopic evidence of relic Archean sediments in the Pitcairn mantle plume. Proceedings of
 379 the National Academy of Sciences of the United States of America, 113, 12952–12956.
 380 doi.org/10.1073

381 El Goresy A., Gillet P., Miyahara M., Ohtani E., Ozawa S., Beck P., and Montagnac G. (2013)
 382 Shock-induced deformation of Shergottites: Shock–pressures and perturbations of
 383 magmatic ages on Mars. Geochimica et Cosmochimica Acta, 101, 233–262.
 384 doi.org/10.1016/j.gca.2012.10.002

385 Fernandes, V.A., Fritz, J., Weiss, B., Garrick-Bethell, I., and Shuster, D. (2013) The bombardment
 386 history of the Moon as recorded by ^{40}Ar - ^{39}Ar chronometry. Meteoritics & Planetary
 387 Science, 48, 241–269. doi.org/10.1111/maps.12054

388 Ferrière, L., Meier, M.M.M., Assis Fernandes, V., Fritz, J., Greshake, A., Barrat, J.-A., Böttger,
 389 U., Bouvier, A., Brandstätter, F., Busemann, H., Korotev, R.L., Maden, C., Magna, T.,
 390 Schmitt-Kopplin, Ph., Schrader, D.L., and Wadhwa, M. (2017) The unique crowdfunded
 391 Oued Awlitis 001 lunar meteorite – A consortium overview. 48th Lunar Planetary Science
 392 Conference, abstract #1621.

393 Fritz, J., Greshake, A., and Fernandes, V. (2017) Revising the shock classification of meteorites.
 394 Meteoritics & Planetary Science, 52, 1216–1232. doi.org/10.1111/maps.12845

395 Fritz, J., Greshake, A., Klementova, M., Wirth, R., Palatinus, L., Assis Fernandes, V., Böttger, U.,
 396 and Ferrière, L. (2019a) Donwilhelmsite, IMA 2018-113. CNMNC Newsletter No. 47,
 397 February 2019, page 199. European Journal of Mineralogy, 31, 197–202.

398 Fritz, J., Fernandes, V., Greshake, A., Holzwarth, A., and Böttger, U. (2019b) On the formation of
 399 diaplectic glass: Shock and thermal experiments with plagioclase of different chemical
 400 compositions. Meteoritics & Planetary Science, 54, 1533–1547.
 401 doi.org/10.1111/maps.13289

402 Garapić G., Jackson, M.G., Hauri, E.H., Hart, S.R., Farley, K.A., Blusztajn, J.S., and Woodhead,
 403 J.D. (2015) A radiogenic isotopic (He-Sr-Nd-Pb-Os) study of lavas from the Pitcairn
 404 hotspot: Implications for the origin of EM-1 (enriched mantle 1). Lithos, 228–229, 1–11.
 405 doi.org/10.1016/j.lithos.2015.04.010

406 Gautron, L., Angel, R.J., and Miletich, R. (1999) Structural characterisation of the high-pressure
 407 phase $\text{CaAl}_4\text{Si}_2\text{O}_{11}$. Physics and Chemistry of Minerals, 27, 47–51.
 408 doi.org/10.1007/s002690050239

409 Gemmi, M. Merlini, M., Palatinus, L., Fumagalli, P., and Hanfland, M. (2016) Electron diffraction
 410 determination of 11.5 Å and HySo structures: Candidate water carriers to the Upper Mantle.
 411 American Mineralogist, 101, 2645.

412 Gemmi, M. Mugnaioli, E., Gorelik, T.E., Kolb, U., Palatinus, L., Boullay, P., Hovmöller, S, and
 413 Abrahams, J.P. (2019) 3D Electron Diffraction: The nanocrystallography revolution. ACS
 414 Central Science, 5, 1315–1329. doi.org/10.1021/acscentsci.9b00394

415 Hirose, K., and Fei, Y. (2002) Subsolidus and melting phase relations of basaltic composition in
 416 the uppermost lower mantle. *Geochimica et Cosmochimica Acta*, 66, 2099–2108.
 417 [doi.org/10.1016/S0016-7037\(02\)00847-5](https://doi.org/10.1016/S0016-7037(02)00847-5)

418 Irifune, T., Ringwood, A.E., and Hibberson, W.O. (1994) Subduction of continental crust and
 419 terrigenous and pelagic sediments: an experimental study. *Earth and Planetary Science*
 420 *Letters*, 126, 351–368. [doi.org/10.1016/0012-821X\(94\)90117-1](https://doi.org/10.1016/0012-821X(94)90117-1)

421 Jarosewich E., Nelen J.A., and Norberg J.A. (1980) Reference samples for electron microprobe
 422 analysis. *Geostandard Newsletters*, 4, 43–47.

423 Kolb, U., Gorelik, T., and Otten, M.T. (2008) Towards automated diffraction tomography: Part II
 424 - Cell parameter determination. *Ultramicroscopy*, 108, 763–772.
 425 doi.org/10.1016/j.ultramic.2007.12.002

426 Litasov, K.D., and Ohtani, E. (2005) Phase relations in hydrous MORB at 18–28 GPa: implications
 427 for heterogeneity of the lower mantle. *Physics of the Earth and Planetary Interiors*, 150,
 428 239–236. doi.org/10.1016/j.pepi.2004.10.010

429 Ma, C., and Tschauner, O. (2017) Zagamiite. IMA 2015-022a. CNMNC Newsletter No. 36, April
 430 2017, *Mineralogical Magazine*, 81, 409.

431 Ma, C., Tschauner, O., and Beckett, J.R. (2017) A new high-pressure calcium aluminosilicate
 432 (CaAl₂Si_{3.5}O₁₁) in martian meteorites: another after-life for plagioclase and connections to
 433 the CAS phase. 48th Lunar Planetary Science Conference, abstract #1128.

434 Matson, D.W., Sharma, S.K., and Philpotts, J.A. (1986) Raman spectra of some tectosilicates and
 435 of glasses along the orthoclase-anorthite and nepheline-anorthite joins. *American*
 436 *Mineralogist*, 71, 694–704.

437 Mugnaioli, E., Gorelik, T., and Kolb, U. (2009) "Ab initio" structure solution from electron
 438 diffraction data obtained by a combination of automated diffraction tomography and
 439 precession technique. *Ultramicroscopy*, 109, 758–765.
 440 doi.org/10.1016/j.ultramic.2009.01.011

441 Nishi, M., Gréaux, S., Tateno, S., Kuwayama, Y., Kawai, K., Irifune, T., and Maruyama, S. (2018)
 442 High-pressure phase transitions of anorthosite crust in the Earth's deep mantle. *Geoscience*
 443 *Frontiers*, 9, 1859–1870. doi.org/10.1016/j.gsf.2017.10.002

444 Palatinus, L., Bráýda, P., Jelinek, M., Hrdá, J., Steciuk, G., and Klementová, M. (2019) Specifics
 445 of the data processing of precession electron diffraction tomography data and their
 446 implementation in the program PETS2.0. *Acta Crystallographica*, B75, 512–522.
 447 doi.org/10.1107/S2052520619007534

448 Palatinus, L., and Chapuis, G. (2007) SUPERFLIP -
 449 a computer program for the solution of crystal structures by charge flipping in arbitrary
 450 dimensions. *Journal of Applied Crystallography*, 40, 786–790.
doi.org/10.1107/S0021889807029238

451 Palatinus, L., Petříček, V., and Corrêa, C.A. (2015a) Structure refinement using precession electron
 452 diffraction tomography and dynamical diffraction: theory and implementation. *Acta*
 453 *Crystallographica*, A71, 235–244. doi.org/10.1107/S2053273315001266

454 Palatinus, L., Corrêa, C.A., Steciuk, G., Jacob, D., Roussel, P., Boullay, P., Klementová, M.,
 455 Gemmi, M., Kopeček, J., Domeneghetti, M.C., Cámara, F., and Petříček, V. (2015b)
 456 Structure refinement using precession electron diffraction tomography and dynamical
 457 diffraction: tests on experimental data. *Acta Crystallographica*, B71, 740–751.
 458 doi.org/10.1107/S2052520615017023

459 Pearson D.G., Brenker, F.E., Nestola, F., McNeill, J., Nasdala, L., Hutchison, M.T., Matveev S.,
 460 Mather, K., Silversmit, G., Vekemans, B., Schmitz, S., Vekemans, B., and Vincze, L.
 461 (2014) Hydrous mantle transition zone indicated by ringwoodite included within diamond.
 462 Nature, 507, 221–224. doi.org/10.1038/nature13080

463 Petříček, V., Dušek, M., and Palatinus, L. (2014) Crystallographic computing system JANA2006:
 464 general features. Zeitschrift für Kristallographie - Crystalline Materials, 229-5, 345–352.
 465 doi.org/10.1515/zkri-2014-1737

466 Plank T., and Langmuir, C.H. (1998) The chemical composition of subducting sediment and its
 467 consequences for the crust and mantle. Chemical Geology, 145, 325–394.
 468 [doi.org/10.1016/S0009-2541\(97\)00150-2](https://doi.org/10.1016/S0009-2541(97)00150-2)

469 Poli, S., and Schmidt, M.W. (2002) Petrology of subducted slabs. Annual Review of Earth and
 470 Planetary Sciences, 30, 207–235. doi.org/10.1146/annurev.earth.30.091201.140550

471 Rozhdestvenskaya, I., Mugnaioli, E., Czank, M., Depmeier, W., Kolb, U., Reinholdt, A., and
 472 Weirich, T. (2010) The structure of charoite, $(\text{K,Sr,Ba,Mn})_{15-}$
 473 $_{16}(\text{Ca,Na})_{32}[(\text{Si}_{70}(\text{O,OH})_{180})](\text{OH,F})_{4.0.n}\text{H}_2\text{O}$, solved by conventional and automated
 474 electron diffraction. Mineralogical Magazine, 74, 159–177.
 475 doi.org/10.1180/minmag.2010.074.1.159

476 Ruzicka, A., Grossman, J., Bouvier, A., and Agee, C.B. (2017) The Meteoritical Bulletin, No. 103,
 477 Meteoritics & Planetary Science, 52, 1014.

478 Sharma, S.K., Simons, B., and Yoder, H.S. (1983) Raman study of anorthite, calcium
 479 Tschermak's pyroxene, and gehlenite in crystalline and glassy states. American
 480 Mineralogist, 68, 1113–1125.

481 Smith, J.V. Anderson, A.T., Newton, R.C., Olsen, E.J., Wyllie, P.J., Crewe, A.V., Isaacson, M. S.,
 482 and Johnson, D. (1970) Petrologic history of the Moon inferred from petrography,
 483 mineralogy and petrogenesis of Apollo 11 rocks. Proceedings of the Apollo Eleven Lunar
 484 Science Conference, 897–925. [https://resolver.caltech.edu/CaltechAUTHORS:20160209-](https://resolver.caltech.edu/CaltechAUTHORS:20160209-101343274)
 485 [101343274](https://resolver.caltech.edu/CaltechAUTHORS:20160209-101343274)

486 Stixrude, L., Koker, N. de, Sun, N., Mookherjee, M., and Karki, B.B. (2009) Thermodynamics of
 487 silicate liquids in the deep Earth. Earth and Planetary Science Letters, 278, 226–232.
 488 doi.org/10.1016/j.epsl.2008.12.006

489 Tomioka, T., and Miyahara, M. (2017) High-pressure minerals in shocked meteorites. Meteoritics
 490 & Planetary Science, 52, 2017–2039. doi.org/10.1111/maps.12902

491 Trønnes, R.G., Baron, M.A., Eigenmann, K.R., Guren, M. G., Heyn, B.H., Løken, A. and Mohn,
 492 C.E. (2019) Core formation, mantle differentiation and core-mantle interaction within Earth
 493 and the terrestrial planets. Tectonophysics, 760, 165–198.
 494 doi.org/10.1016/j.tecto.2018.10.021

495 White, W.M. (2015) Isotopes, DUPAL, LLSVPs, and Anekantavada. Chemical Geology, 419, 10–
 496 28. doi.org/10.1016/j.chemgeo.2015.09.026

497 Wieczorek, M.A., Jolliff, B.L., Khan, A., Pritchard, M.E., Weiss, B.P., Williams, J.G., Hood,
 498 L.L., Righter, K., Neal, C.R., Shearer, C.K., McCallum, I.S., Tompkins, S., Ray Hawke,
 499 B., Peterson, C., Gillis, J.J., and Bussey, B. (2006) The constitution and structure of the
 500 lunar interior. Reviews in Mineralogy and Geochemistry, 60 (1), 221–364.
 501 doi.org/10.2138/rmg.2006.60.3

502 Wilhelms, D.E. (1987) The geological history of the Moon. US Geological Survey Professional
 503 Paper 1348, pp 302. [doi: 10.3133/pp1348](https://doi.org/10.3133/pp1348)

504 Wilhelms, D.E. (1993) To a rocky Moon: A geologist's history of lunar exploration. The University
505 of Arizona Press, pp. 477.

506 Wittmann, A., Korotev, R.L., Jolliff, B.L., Nishiizumi, K., Jull, A.J.T., Caffee, M.W., Zanetti M.,
507 and Irving, A.J. (2019) Petrogenesis of lunar impact melt rock meteorite Oued Awlitis 001.
508 Meteoritics & Planetary Science, 54, 2167–2188. doi.org/10.1111/maps.13218

509 Wood, J., Dickey, J.S.Jr., Marvin, U., and Powell, B.N. (1970) Lunar anorthosites. Science, 167,
510 602–604. doi.org/10.1126/science.167.3918.602

511

Figure captions

Figure 1: Backscattered-electron (BSE) image showing a petrographic overview of the lunar meteorite Oued Awlitis 001 (NHMV-O104). Large plagioclase clasts (pl clast) are embedded in a matrix composed of olivine (ol), pyroxene (px), plagioclase (pl), and silica (not indicated).

Figure 2: Backscattered-electron (BSE) image showing a) a shock melt pocket with needles of donwilhelmsite. The grey host rock is mainly composed of anorthite with bright minerals representing olivine and pyroxene. Dark regions are cracks on the surface of the polished thick section. b) BSE image showing bundles of needle-like (acicular) donwilhelmsite crystallized in a ~100 μm wide shock melt pocket of anorthitic chemical composition. The donwilhelmsite needles are surrounded by a darker halo. c) Bright field TEM image showing an almost defect free donwilhelmsite crystal. The dark upper left corner is the platinum strip holding the sample.

Figure 3: Ca, Al, and Fe elemental maps and backscattered electron (BSE) image showing needles of donwilhelmsite within a shock melt pocket. Elemental maps of Fe and Mg (not shown) reveal chemical inhomogeneity within the anorthositic-like shock melt pocket, likely related to melted pyroxene or olivine grains.

Figure 4: Raman spectra of donwilhelmsite and the glass composing the shock melt pocket. The donwilhelmsite spectra shows peaks at 280, 420, 500, 618, 850, and 912 cm^{-1} together with spectral contributions from the surrounding glass halo providing broad features in the 500 to 560 region and at ~1015 cm^{-1} Raman shift. The shock melt pocket displays a Raman spectra with broad hump with maxima at ~500 and ~560 cm^{-1} and a broad hump with a maxima at ~985 cm^{-1} Raman shift.

Figure 5: Precession electron diffraction tomography (PEDT). Displayed are sections through the experimental diffraction dataset 180520-2 in three orientations with the unit cell marked.

Figure 6: Structure of donwilhelmsite. a) The structure is composed of b) octahedral M1-layers (dark blue) occupied by Al and Si in 1:2 ratio. c) The interlayers, contain octahedral M2-positions (grey) fully occupied by Al, tetrahedral positions (T, grey) half occupied by Al, and cavities occupied by Ca (green).

Table 1 | Chemical composition of the shock melt pocket given as an average of 10 electron microprobe analyses (Melt) and their standard deviation (S.D.). The chemical composition of the glass halo rimming donwilhelmsite (Gl) and for donwilhelmsite (DW) were obtained by TEM-EDS analytics.

	Melt	S.D.	Gl	DW
SiO ₂	44.0	0,75	60.7	32.6
Na ₂ O	0.35	0.06		
TiO ₂	0.10	0.04		
K ₂ O	0.01	0.01		
Cr ₂ O ₃	0.04	0.02		
Al ₂ O ₃	35.4	1.23	20.8	52.7
MgO	0.52	0.18		
MnO	0.01	0.02		
CaO	18.9	0.51	18.5	15.0
FeO	1.09	0.34		
Total	100.4	0.41	100.0	100.3



Table 2 | Chemical data (in *weight % of oxides* and *atoms per formula unit = apfu*). For donwilhelmsite, the empirical formula as calculated on the basis of 7 cations is $\text{Ca}_{1.02}\text{Al}_{3.92}\text{Si}_{2.06}\text{O}_{11}$, and the simplified formula is $\text{CaAl}_4\text{Si}_2\text{O}_{11}$.

	Al₂O₃	SiO₂	CaO	Al	Si	Ca
	wt%	wt%	wt%	7 apfu	7apfu	7 apfu
sp-01	52.3	32.1	15.7	3.9	2.0	1.1
sp-02	54.0	32.6	14.1	4.0	2.1	1.0
sp-03	46.8	35.2	17.7	3.5	2.3	1.2
sp-04	52.9	34.1	13.9	3.9	2.1	0.9
sp-05	54.0	32.2	14.3	4.0	2.0	1.0
sp-06	51.5	33.1	15.6	3.8	2.1	1.1
sp-07	52.8	32.7	14.9	3.9	2.1	1.0
sp-08	53.3	31.0	15.6	4.0	2.0	1.1
sp-09	53.2	31.6	15.3	4.0	2.0	1.0
sp-10	56.0	31.4	13.3	4.1	2.0	0.9
average	52.7	32.6	15.0	3.9	2.1	1.0
std. dev.	2.4	1.3	1.2	0.2	0.1	0.1
min.	46.8	31.0	13.3	3.5	2.0	0.9
max.	56.0	35.2	17.7	4.1	2.3	1.2

Table 3 | Comparison of crystal data with hexagonal crystal system. Diffraction data of the here described new mineral was determined by precession electron diffraction tomography (PEDT), X-ray diffraction data from Gautron et al. (1999) are obtained on single crystals and Akaogi et al. (2009) used powder samples. The synchrotron diffraction patterns of micrometer-sized high aluminum silica (HAS) zagamiite grains were consider similar to powder-like samples (Ma et al. 2017). The cell parameters of these hexagonal crystals are given as a and c in [Å] Angstrom and the cell volume $V = a^2c \sin(60^\circ)$ in [Å³]. The numbers in parentheses () represent the estimated standard deviations in the last digit. *Unit cell parameters from electron diffraction tomography (EDT) are known to have distortions and lower accuracy (Kolb et al., 2008). Z is the number of formula units per unit cell. The calculated density of donwilhelmsite is 3.903 [g/cm³].

Composition	Space group	a [Å]	c [Å]	V [Å ³]	Z	Reference
Donwilhelmsite CaAl₄Si₂O₁₁	$P6_3/mmc$	5.42 (1)	12.70 (3)*	323(4)	2	This work
synthetic CaAl₄Si₂O₁₁	$P6_3/mmc$	5.4223 (4)	12.7041 (6)	323.28 (5)	2	Gautron et al. 1999
synthetic CaAl₄Si₂O₁₁	$P6_3/mmc$	5.4239 (2)	12.6805 (5)	323.06 (3)	2	Akaogiet al. 2009
Zagamiite CaAl₂Si_{3.5}O₁₁	$P6_3/mmc$	5.403 (2)	12.77 (3)			Ma et al. 2017

Table. 4 | Characteristics of cation coordination.

position	occupancy	BVS ¹	ECON ²	average distance to coordinating oxygen atoms [Å]	average distance of synthetic CAS [Å] [2]
Ca	Ca	1.816(3)	11.8945	2.6723	2.671
M1	Si1 (2/3)	3.513(7)	5.9876	1.8325	1.833
	Al1 (1/3)	3.61(1)			
M2	Al2	2.956(6)	5.6976	1.9159	1.918
T	Al3 (1/2)	3.15(2)	3.8164	1.7456	1.724

¹BVS - Bond Valence Sum; ²ECON - Effective Coordination Number.

566 **Table. 5 | Analytical conditions for donwilhelmsite.**

Data collection	
Radiation type	electrons, 120 kV
Wavelength [Å]	0.0335
Precession angle φ [°]	1.0
Illuminated area diameter [nm]	1 000
Resolution [Å]	0.7150
No of recorded frames	101
Completeness	100
No. of refined reflections - all/observed [$I > 3\sigma(I)$]	3 639/2 574
Dynamical structure refinement	
g^{\max} [Å ⁻¹], S_g^{\max} (matrix), S_g^{\max} (refine), R_{Sg} , N_{or}	1.6, 0.01, 0.1, 0.4, 128
R1(F), wR(F), GOF - (obs/all) [%]	8.95/11.91, 10.00/10.12, 4.77/4.06
No. of refined parameters	127

567 ^a $RI = \Sigma|F_o|/|F_c|/\Sigma|F_o|$; ^b $wR = [\Sigma w(F_o^2 - F_c^2)^2/\Sigma w(F_o^2)^2]^{1/2}$; ^c $GOF = [\Sigma w(F_o^2 - F_c^2)^2/\Sigma$
568 $w(F_o^2)^2]^{1/2}$

Fig. 1

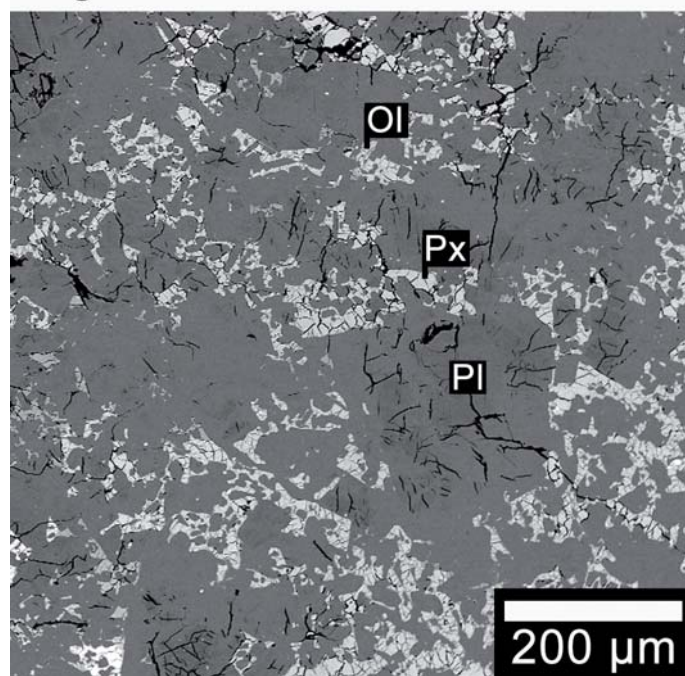


Fig. 2

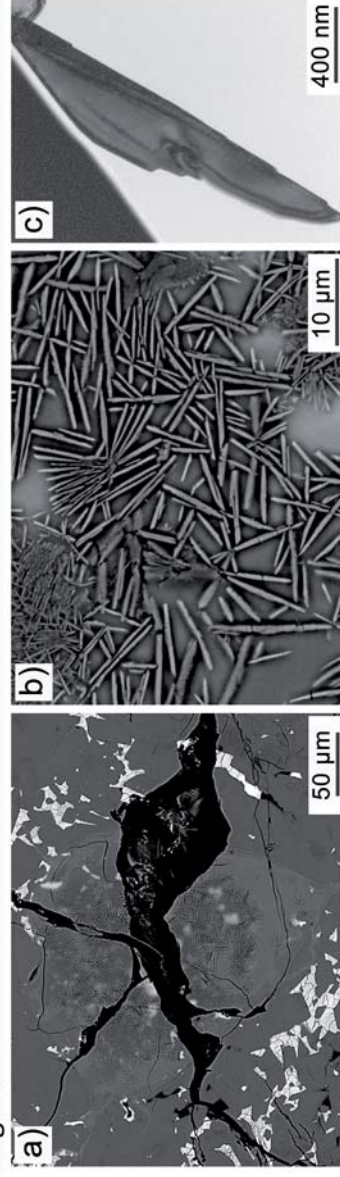


Fig. 3

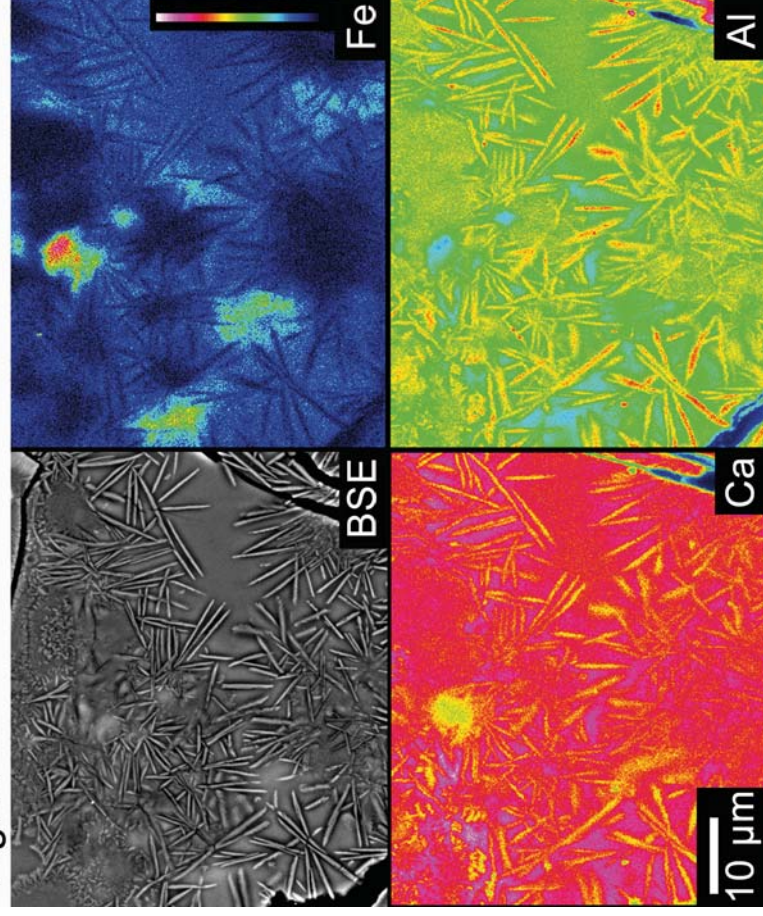


Fig. 4

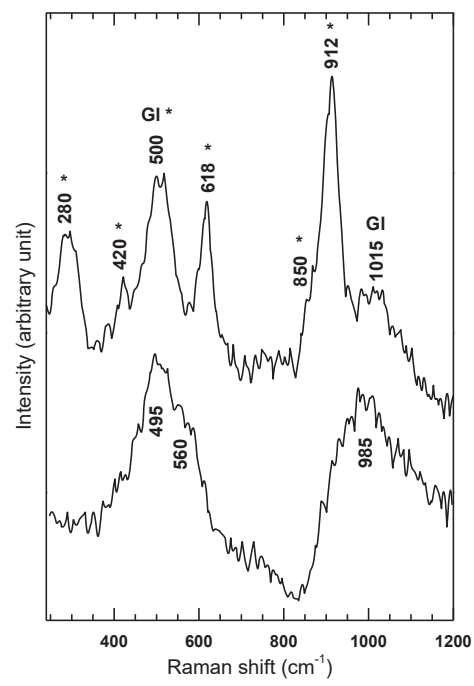


Fig. 5

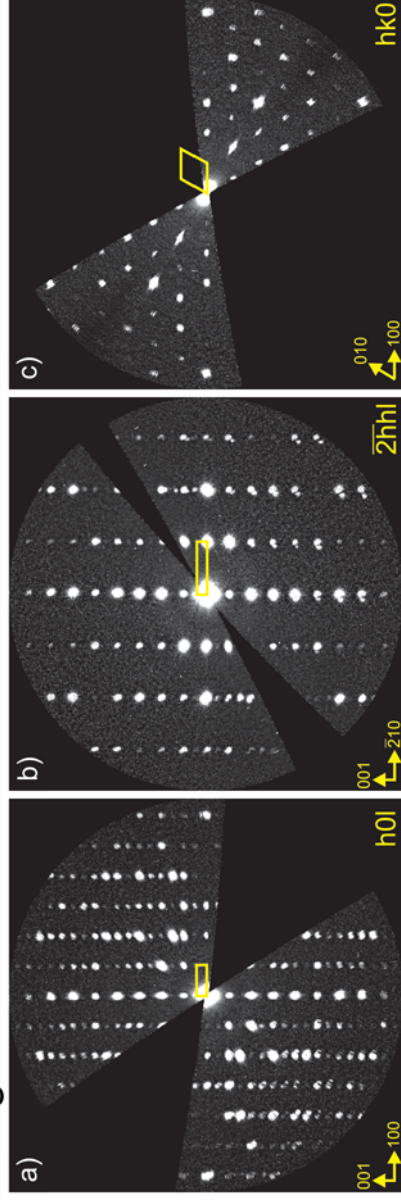


Fig. 6

